POLITECNICO MILANO 1863

DIPARTIMENTO DI MECCANICA

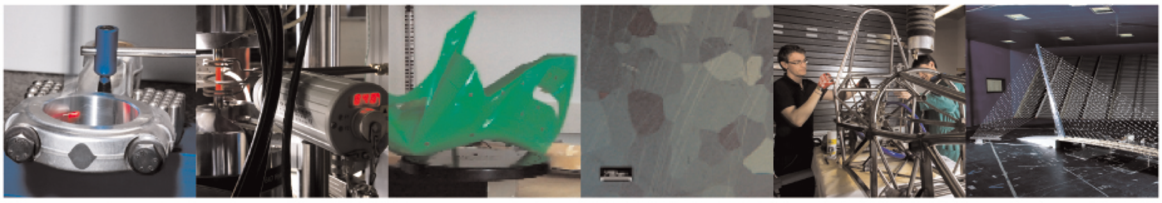

Insights into the printing parameters and characterization of thermoplastic polyurethane soft triply periodic minimal surface and honeycomb lattices for broadening material extrusion applicability

Sala, R;Regondi, S;Graziosi, S;Pugliese, R

This is a post-peer-review, pre-copyedit version of an article published in Additive Manufacturing. The final authenticated version is available online at: https://doi.org/10.1016/j.addma.2022.102976

Insights into the printing parameters and characterization of thermoplastic polyurethane soft triply periodic minimal surface and honeycomb lattices for broadening material extrusion applicability

Riccardo Sala[1,‡], Stefano Regondi[1], Serena Graziosi[2,*], and Raffaele Pugliese[1,‡,*]

[1]NeMO Lab, ASST Niguarda Cà Granda Hospital, Milan, Italy.

[2]Department of Mechanical Engineering, Politecnico di Milano, Milan, Italy.

[‡]These authors contributed equally

[*]Corresponding author at: raffaele.pugliese@nemolab.it (R.P.), serena.graziosi@polimi.it (S.G.)

Abstract

Lattice structures with triply periodic minimal surfaces (TPMS) built using flexible materials are soft porous solids applicable in various fields, including biomedicine and tissue engineering. Such structures are also relevant for material extrusion additive manufacturing (MEAM), whose wide diffusion is pivotal to fostering their spread. Although design approaches are available to exploit the potential of soft TPMS, there are still manufacturing constraints that lead to practical limits on the shape and size of the structures that can be produced due to the complexities related to printing flexible materials. Besides, the computational models investigating the effect of cell type, the surface-to-volume fraction, and the combination of different periodic surfaces (i.e., graded or hybrid) on the mechanical behavior of these lattices are design aspects still debated. Here, the capabilities of MEAM to produce tailored soft lattice structures are explored by combining a design tool, numerical analyses, and mechanical testing using thermoplastic polyurethane (TPU) as feedstock material. The study addresses design issues, delves into optimum printing parameters, and analyzes a set of numerical parameters, which can be used for designing specific structures with tunable mechanical behavior, useful for healthcare and bioengineering. The printing parameters of three lattices, i.e., schwartz-P, gyroid, and honeycomb, with unit cell sizes spanning from 3 to 12 mm were studied. Their mechanical behavior was investigated using FEM simulations and mechanical testing. Lastly, the printability of graded and hybrid lattices with enhanced bearing-load capabilities have been demonstrated. Altogether, our findings addressed multiple challenges associated with developing soft lattice scaffolds with MEAM that can be used to fabricate innovative-engineered materials with tunable properties.

Keywords: fused filament fabrication (FFF); design for additive manufacturing; thermoplastic polyurethane (TPU); finite element analysis (FEM); lattice structures; triply periodic minimal surfaces (TPMS).

1. Introduction

The field of engineering design lattice structures is continuously growing in different sectors such as biomedical, tissue engineering, orthopedics, aerospace, and automotive [1-9]. Nature has played a crucial role for scientists to understand and explore such structures [10-12]; just think of the geometry, shape, and mechanical properties of shells, shark teeth, honeycomb, cancellous bone, and marine sponges. Indeed, nature has found a fascinating way to use geometric lattice design principles, allowing structures (or molecules) to hierarchically self-assemble from nano- to meso-scale level, thus leading to exceptional properties [12]. Among the above-mentioned structures, lattices with periodic minimal surfaces and negative Gaussian curvature are widely investigated due to their lightweight nature, and ability to absorb compressive energy, exchange heat, and dampen acoustic vibrations [13-15]. However, the sophisticated geometry of these lattice structures has proven challenging to fabricate by conventional methods. The emerging capability of material extrusion additive manufacturing (MEAM) could solve some of the bottlenecks, making such lattice structures attractive for different applications [16-21]. According to specific needs, with MEAM these structures can be fabricated in various materials, from polymers to hydrogels, up to metal alloys [22, 23]. Among this wide range of materials, those that allow the creation of soft lattice structures, i.e., lattices that undergo large elastic deformations [24], can be of high interest in different areas of healthcare. Their flexibility and tunability (from micro to macro-scale), could make soft lattices valid substitutes for polyurethane-based foams [25], with the aim to provide wearable and personalized support structures for patients with specific clinical needs. For instance, as recently reported by Holmes and colleagues [26], 3D printed soft gyroid lattice metamaterials can have a significant role in the treatment of decubitus ulcers or pressure injuries, as they have the ability to reproduce the mechanical behavior of soft padding foams already on the market (e.g. EN 36-90, EN 40-230, and MA 36-600 manufactured by Dunlop Foams). In addition, the ability to finely control the unit cell sizes, the surface-to-volume fraction, and the printing processes are essential requirements to guarantee the fabrication of soft porous structures for 3D cell culture [27] and therefore broadening the applications of soft lattices via MEAM. Such parameters ensure proper cellular adhesion, colonization within the scaffolds, a good permeability of fluid media and oxygen, and the possibility of vascularization, thus overcoming the current limitations of the bioprinting technique [28]. Also, the feasibility of using size-programmable 3D printed soft lattices could be helpful for pharmaceutical applications to test and achieve customized and controlled drug-delivery systems, adapting the drug posology to the patient simply by changing the 3D design of the structures [29]. Finally, the possibility of prototyping through MEAM customized and tailored soft orthoses and cushions [30] could pave the way for their use in neurodegenerative and neuromuscular pathologies, such as spinal cord injury (SCI), traumatic brain injury (TBI), amyotrophic lateral sclerosis (ALS), and spinal muscular atrophy (SMA).

Nevertheless, although different design approaches have been proposed for such structures [31-36], a critical challenge that still needs to be addressed for the design of lattices is to choose the appropriate lattice design variables, such as cell type, unit cell size, and volume fraction in relation to the selected material. Furthermore, using MEAM, there are still not enough explored manufacturing constraints regarding the minimum and maximum length of the periodic minimal surfaces, self-supporting sloping angles, and minimum diameters or thicknesses that lead to practical limits on the shape and size of structures that can be produced using flexible materials.

Among these, it is important to emphasize the feasibility of producing through FFF supportless lattice structures, particularly when printing hyperelastic material. As claimed in [37, 38], one of the major challenges in the AM process is the removal of unwanted support structures from the lattice, since they consume extra material and increase printing time, and energy for manufacturing. To overcome this issue, the authors reported the design of a shell-shaped lattice structure inspired by sea urchin morphology that can be additively manufactured by MEAM without requiring any support structures useful for possible application in customized shoe midsoles, ski boots, tires, automotive crush boxes, or any other energy-absorbing structures. They highlighted that such supportless lattice did not show sagging or failure in both the experimental test and predictive model, thus reducing the manufacturing and post-processing time, saving a significant amount of material without compromising quality.

Lastly, the computational models applied to investigate the effect of cell type, the surface-to-volume fraction, and the combination of different periodic surfaces (i.e., graded or hybrid) on the mechanical behavior of these soft structures are still debated and poorly understood.

For these reasons, in this study, we investigated the capability of MEAM to produce tunable soft lattice structures by combining the Functional Lattice Package (FLatt Pack) program with finite element method (FEM) (1) to address design issues, (2) assess the optimum processing parameters for Thermoplastic Polyurethane (TPU, 80 Shore A) soft lattices, and (3) predict their mechanical behavior, useful for materials science, tissue engineering, and biomedical implants. Paying attention to the available polymers for this purpose, we selected the TPU because of its high flexibility and deformability. Combined with the proper lattice architecture, these characteristics might increase compressive loading efficiency, energy absorption, and crashworthiness. These capabilities can be relevant for developing innovative lightweight wearable solutions or scaffolds for the healthcare sector. The FLatt Pack program, created by Maskery [39], possesses several peculiar features for the development of lattice structures, including: (1) twenty-three lattice cell types covering a broad range of pore connectivity, structural anisotropy, and surface area; (2) a graphical user interface (GUI) presenting the lattice design stages in a sequential manner; (3) surface-to-volume estimation; (4) relative modulus estimation; (5) the possibility of creating graded structures; (6) the option to export designs in appropriate formats for 3D printing and finite element simulation.

Through this software tool, we generated three lattice structures that represent the focus of our study; the so-called schwartz-P, gyroid, and honeycomb structures. Even if the honeycomb is not classifiable as a TPMS, it was studied for the following reasons: it has a geometrically simple but effective periodic shape; it is a wall-based structure which means that surfaces and not beams represent its main constitutive features as in the TPMS; its stiffness and wall-based shape can be attractive for the design of scaffolds for the repair of human bone defects [40].

Each TPU-based structure was 3D printed with different unit cell sizes, spanning from 3 to 12 mm (equal to a volume fraction ranging from 0.14 to 0.56). The intent was to explore their behavior at different dimensional levels and thus for multiple applications, keeping the same thickness of 1 mm for all samples. To assess the printability limitation and the soft lattices manufacturability, we studied the effects of the following variables: printing temperature, retraction speed, retraction distance, printing speed, wipe distance, extrusion multiplier, and fan speed. Further, by using finite element (FE) simulation either in linear or non-linear hyperelastic models, we examined the behavior of these lattices under compressive loading. A systematic investigation into the mechanical behavior of each manufactured soft lattice structure was performed experimentally to validate the FE simulation data.

Since graded and hybrid structures are strategic for designing material-efficient solutions [41-45], the optimized print parameters were used to probe the printability and mechanical behavior of a gyroid with a variable volume fraction distribution and of a honeycomb with a hybrid design.

Ultimately, such integrated design approach, which includes FLatt Pack, FEM method, mechanical testing, and 3D printing allowed us to engineer well-defined and tailorable soft lattice structures, which can be used as a starting point for building innovative material-driven properties (e.g., acoustic, thermal, energetic), scaffolds for targeted tissues or 3D cell cultures, light-weighting soft orthosis (e.g., non-invasive ventilation masks for mechanical ventilation, foot-beads, wrist brace), and medical implants (e.g., cardiac stents, padding cushion, drug-delivery systems).

These thorough investigations can be a valuable strategy to effectively push the boundaries of the fused filament fabrication (FFF) process for soft lattice structures. Indeed, optimizing the FFF printing parameters can allow a printing resolution adequate to print flexible lattice microstructures with the desired level of accuracy. Besides, it can push forwards the use of biocompatible and bioabsorbable polymers, more suitable for biomedical applications, as the feedstock is safer and easier to handle and requires no further post-processing. The FFF process has the chance to guarantee more versatility compared to, for example, the laser sintering (SLS) or the stereolithography (SLA) processes.

2. Materials and Methods

2.1. Materials

Thermoplastic polyurethane filament (TPU) 80 Shore A with a 2.85 mm diameter (FlexMark8, Treed Filaments, Italy) was used as the feedstock material, without further modifications. All materials were handled with gloved hands, and standard surface analysis laboratory practices were followed to minimize any possible contamination.

2.2. Design of lattice structures

The honeycombs were generated using Autodesk Inventor software (Autodesk 2020, McInnis Parkway San Rafael, CA, USA), selecting a wall thickness of 1 mm for each designed cell and sketching a regular hexagon as base for the extrusion. Four different cell sizes were chosen for the analysis, ranging from 3 mm to 6 mm. The model height has been set equal to the cell size, thus increasing the model height as the cell size increases. The schwartz-P and gyroid structures were generated using the Functional Lattice Package (FLatt Pack) program (2021, University of Nottingham) capable of designing lattice structures starting from the size of one cell and its volume fraction [39]. Before introducing the surface equations used to generate such lattice structures, we introduce some terms related to their design. The first of them is the periodicity κ calculated as follows:

$$\boldsymbol{\kappa_i = 2\pi n_i} \qquad (1)$$

where *i* refers to the *x*, *y*, and *z* directions and n_i are the number of cell repetitions in each of those directions.

A shorthand notation for sine and cosine periodic function is then defined, as follows:

$$\boldsymbol{S_i = sin\left(\kappa_i \frac{i}{L_i}\right)} \quad (2)$$

and

$$\boldsymbol{C_i = cos\left(\kappa_i \frac{i}{L_i}\right)} \quad (3)$$

where L_i is the absolute size of the lattice structure in the direction *i* of interest.

Then, the approximated functions to obtain the schwartz-P (U_P) and gyroid (U_G) structures are calculated as follows:

$$\boldsymbol{U_P = C_x + C_y + C_z - t} \quad (4)$$

$$\boldsymbol{U_G = C_x S_y + C_y S_z + C_z S_x - t} \quad (5)$$

where $C_{x,y,z}$ and $S_{x,y,z}$ refer to the periodic sine and cosine function described above and t is an arbitrary constant related to the volume fraction of the generated lattice structure.

Four different unit cell sizes were adopted (6, 8, 10, and 12 mm) and fine-tuned to obtain walls of 1 mm thickness. The selection of the geometry size was closely related to the ability of the FFF printer to print them with the proper tuning of the selected printing parameters (see Section 2.4).

2.3. Design of graded and hybrid lattice structures

The three-layered hybrid structure was created using Autodesk Inventor, combining honeycomb oriented orthogonally with respect to the *y-z* and to *x-y* planes, in such a way that the orientation was *x*-direction in the top and bottom thirds, and *z*-direction in the middle third. The unit cell size was set as 6 mm, and 3 × 2 cells were used for the top and bottom thirds, while 5 × 3 cells for the middle third. The thickness of the wall model was set to 1 mm and exported as "stp" file for FE simulation. Instead, the graded gyroid lattice structure was generated using FLatt Pack selecting a linear gradient variation of the volume fraction from 0.23 to 0.46 (corresponding to a thickness variation from 1 mm to 2 mm). A 2 × 2 × 2 lattice was generated and the model was exported as an input file (.inp) for the FE simulations. In both cases, considering the aim of the study, we controlled the model generation by monitoring the resulting thickness of the 3D model main features.

2.4. Selection of the printing parameters

All lattice structures were 3D printed using the FFF Delta WASP 2040 Industrial X (World's Advanced Saving Project, Massa Lombarda, Italy) machine adopting the WASP FLEX direct drive extruder suitable for flexible materials up to Shore 80 A. The printer has a maximum building volume of 200 × 200 × 400 mm, and a layer resolution of 50 μm, corresponding to a nozzle with 0.4 mm of diameter. The following parameters were kept constant: nozzle diameter (0.4 mm), infill (100%), and layer height (0.15 mm). The following parameters were tuned to probe the optimum printing combination: printing temperature, retraction speed, retraction distance, printing speed, wipe distance, extrusion multiplier, and fan speed. Each scaffold was modeled using FLatt Pack (except for honeycomb, which was modeled with Autodesk Inventor® software), then exported in stereolithography (.stl) format and sliced using the Simplify3D® software. To ensure the adhesion of the scaffolds to the surface of the printing platform, a 3D glue stick (Magigoo™, Swieqi, Malta) was used.

2.5. Finite element analysis

Finite Element (FE) simulations were performed to study the mechanical behavior of the three cell-based structures. The honeycomb structures were exported as "stp" files from Autodesk Inventor software and then imported as continuous solid parts. Instead, schwartz-P and gyroid structures obtained through the FLatt Pack program were uploaded for the FE simulations as input (.inp) files (already meshed and ready to be processed, Figure S1). Two different types of simulations were conducted considering the behavior of the TPU material as linear or hyperelastic. In the linear elastic condition, the Young's modulus and Poisson's ratio of TPU were assumed to be 26 MPa and 0.45, respectively, as reported previously [46, 47]. A three-variable Mooney-Rivlin model was used for nonlinear hyperelastic simulations, with a C_{01} = 0.363 MPa, C_{10} = 2.93 MPa, and D = 0 to simulate incompressibility of the material, as previously reported [48, 49].

The compression simulation was performed by imposing the correct boundary conditions on two planes of the imported lattice structure, particularly on two parallel faces, oriented orthogonally with respect to the direction of interest to calculate the Young's modulus. A reference point was applied to the fixed surface, and linked with the whole area with a tie rod type Multi-Point Constraints (MPC) to correctly extract the reaction force value without further point integrations. A second reference point was then linked with a tie-type MPC with the moving face (i.e., the one subjected to the imposed displacement) to extract the corresponding displacement value of the whole surface. The calculation of the Young's modulus was performed as follows:

$$\boldsymbol{E_i} = \frac{\sigma_i}{\varepsilon_i} \quad (6)$$

where E is the equivalent Young's modulus in the direction i of interest; σ is the equivalent stress, calculated as the ratio between the reaction force and the equivalent area; ε is the strain, calculated as the ratio between the imposed displacement and initial length of the lattice in the direction i.

The boundary conditions were applied through the two reference points. An encaster is applied to the first reference point. For the second reference point an initial displacement of 5% of compressive strain in the direction of interest was applied.

The hybrid honeycomb structure was imported as a single continuous part. For a faster calculation, the model was cut in a quarter of the whole piece, to take advantage of the geometrical symmetry;

two shell parts were also generated to simulate a compression machine moving and fixed surfaces. The two planes were treated as 2D discrete rigid parts; thus no material selection was necessary. Then, boundary conditions were applied to the whole model, imposing a vertical displacement of the upper part equal to 40% of the model height and an encaster constraint in the bottom part. The symmetries of the simplified model need to be represented with two additional boundary conditions, in the *x* and *z* directions, to allow the model to behave like the not-simplified structure. See Supporting Information for further details.

2.6. Mechanical testing

Quasi-static compression tests were performed using the MTS Synergy 200 testing machine equipped with a 1 kN load cell to experimentally characterize the scaffolds' behavior and validate the numerical models. Three repetitions were tested for all homogenous samples, while one sample was analyzed for the hybrid honeycomb and the graded gyroid. All specimens were tested with a crosshead speed of 5 mm/min.

2.7. Scanning electron microscopy (SEM)

Sagging, improper layer adhesion, and porosity of 3D printed honeycomb, schwartz-P, and gyroid structures were observed using a field emission scanning electron microscopy (Zeiss EVO 50) operating at 30 kV. All specimens were sputter coated with gold prior to examination to ensure better conductivity and prevent the formation of electrostatic charges.

3. Results and Discussion

3.1. Soft lattice structures design and printability

The honeycomb, schwartz-P, and gyroid unit cells were generated as periodic matrices [50] (Figure 1 A-C). Then, they were converted to three-dimensional cuboid structures starting from the size of one cell and its volume fraction (Figure 1 D-F) (see Section 2.2 for further details). Furthermore, taking advantage of the FLatt Pack "surface-to-volume estimation" feature, it was possible to estimate the surface-to-volume ratio for each cell over a range of volume fractions and cell sizes (Figure 1 G-I). This feature can provide a relevant design criterion not only to fine-tune the structures, but also when the intended application for the selected lattice involves the interaction of its surface with a specific environment (e.g., for biological scaffolds, where the amount of surface determines the number of cells that can attach and grow there, or for medical implants where heat transfer across the surface to a fluid medium must be ensured).

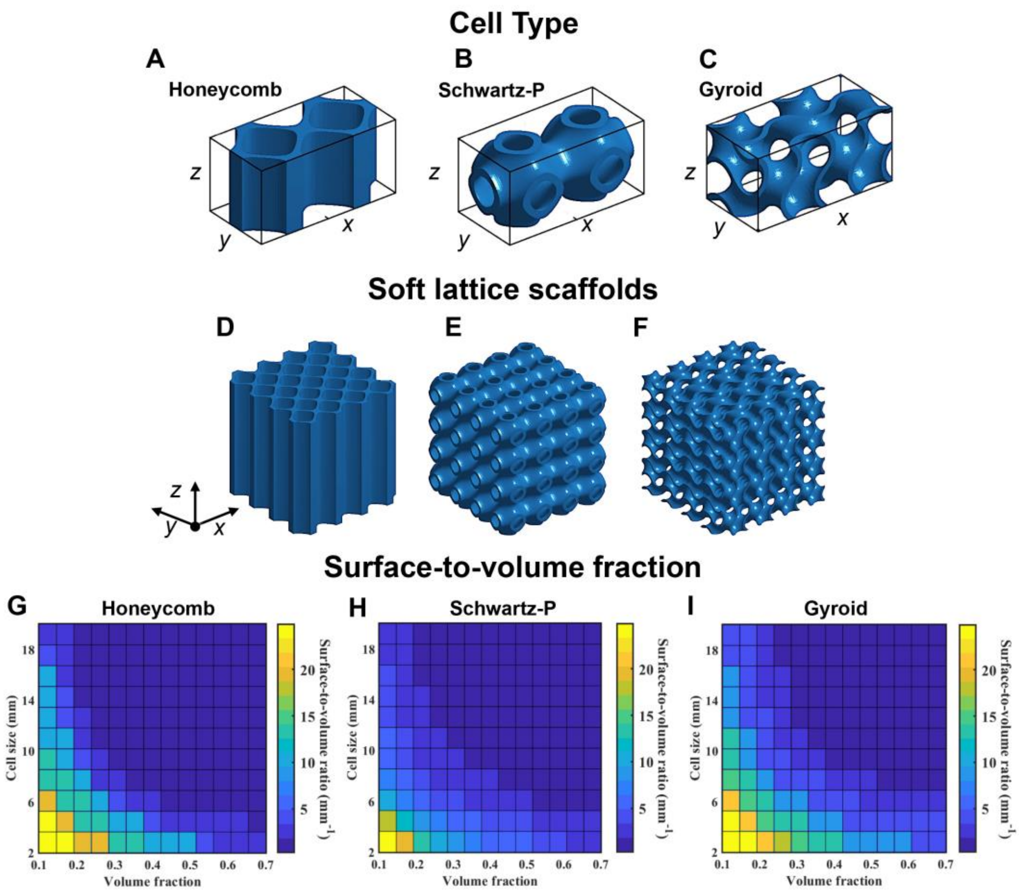

Figure 1. Unit cell geometry based on (A) honeycomb, (B) schwartz-P, (C) gyroid, and (D-F) corresponding cuboid matrix. (G-H) The surface-to-volume ratio for each tested cell obtained through FLatt Pack "surface-to-volume estimation" feature.

According to the literature due to topological constraints [51], the minimum unit cell size allowed for printing honeycomb is 3 mm (volume fraction of 0.56), whereas for schwartz-P and gyroid is 6 mm (volume fraction of 0.28 and 0.46, respectively). Instead, the maximum value of unit cell achievable is 6 mm for honeycomb, and 12 mm for schwartz-P and gyroid. Then, once the preliminary unit cells sizing has been tuned, such lattices were 3D printed. An overview of the cell sizes and related volume fractions is provided in Table 1.

Honeycomb			Schwartz-P			Gyroid		
Unit cell size (mm)	**Volume fraction**	**Void fraction**	**Unit cell size (mm)**	**Volume fraction**	**Void fraction**	**Unit cell size (mm)**	**Volume fraction**	**Void fraction**
3	0.56	44%	6	0.28	72%	6	0.46	54%
4	0.44	56%	8	0.21	79%	8	0.35	65%
5	0.36	64%	10	0.17	83%	10	0.28	72%
6	0.31	69%	12	0.14	86%	12	0.23	77%

Table 1. The unit cell sizes allowed for the 3D printing of honeycomb, schwartz-P, and gyroid lattices, and the corresponding volume fraction and void fraction percentage values.

Based on many tests carried out, all structures were successfully 3D printed with an optimized nozzle temperature of 230 °C (Figure S2). The optimized parameters for the honeycomb with a unit cell size of 3 mm were an extrusion width of 0.65 mm, a retraction distance of 1 mm, and a retraction speed of 2,400 mm/min. Details concerning the printing path of honeycomb with a unit cell size of 3 mm are provided in Figure S3. A greater retraction distance was not achievable due to the direct drive extruder used to print the TPU through the Delta WASP 2040 Industrial X (see Section 2.4); instead, a lower value resulted in debris and lumps of filaments inside the honeycomb cells, thus turning in a reduced surface quality of the structure. The optimum printing speed was 1,100 mm/min, as higher speeds did not allow proper material deposition and distorted honeycombs were generated. However, we must recall that using a slower print speed while ensuring good printability increases production times considerably. Lastly, to promote good adhesion of the first layer, a build plate temperature of 50 °C was selected, and the cooling system was turned “off”, as we observed that the contribution of the fan during the printing process caused early cooling of the TPU filament, leading to the layer’s detachment.

For unit cells from 4 mm up to over 6 mm, we used the same process parameters as the 3 mm unit cell size. In these cases it was possible to increase the printing speed up to 3,000 mm/min because (as shown in Figure 1 G, and Table 1) increasing the unit cell size decreases the volume fraction. It is thus possible to obtain a good surface quality of the structure without debris and lumps of filaments (Figure S2A), and, at the same time, decrease production times.

For schwartz-P the smaller unit cell successfully 3D printed was 6 mm (Figure S2B), with a retraction speed of 3,000 mm/min to avoid debris on the structure's surface and a printing speed of 1,000 mm/min. We noticed that a faster printing speed resulted in an incorrect material deposition during the bridging phase, thus generating voids and weakening the overall structures. Conversely to the honeycomb structures, to promote a good adhesion of the schwartz-P structures to the build plate, the first layer speed was decreased to 50% and a 120% layer width was selected; also, a 20% fan speed was used because it avoided the local structure overheating. As schwartz-P geometry requires the formation of small bridges between cells, the wipe distance of 2 mm length was enabled to prevent additional debris during printing. Using this method, the nozzle could travel for an extra 2 mm length on the same path, avoiding the spread of the material over the entire lattice's surface.

Also in this case, as for the honeycomb structures, with the increase in the unit cell size, it was possible to increase the printing speed up to 2,400 mm/min to obtain the same result in terms of surface quality of lattices. However, some drawbacks occurred during the bridging procedure (not detected for 6 mm cells) for much larger unit cells due to the loss of material during the creation of the cantilever structure. To overcome this issue, the extrusion multiplier was set to 1.1 while keeping the print speed unchanged, thus allowing building support-less schwartz-P structures.

The same printing parameters used for schwartz-P were used for the gyroid structures with the unit cell of 6 mm, except for the wipe nozzle option in which a wipe distance of 0.5 mm was used to avoid loss of filaments on all surfaces of the final construct. Once again, for cells larger than 6 mm, the print speed was increased up to 2,400 mm/min, with no surface or geometric quality loss (Figure S2C). However, unlike the schwartz-P structures, there was no need to use the extrusion multiplier when creating the cantilever walls of the cells. For the sake of clarity, an overview of the used printing parameters is provided in Table S1.

Based on an initial visual inspection and as shown in Figure 2 A-C, the tuned printing parameters led to satisfactory results concerning the overall printing quality of the samples considering the flexible nature of the filament and the complexity of the structures. Looking at the upper surface of all lattice structures, a uniform way of filling can be seen without debris, stringing inside the unit cell, and long lumps of filaments. In addition, there are no visible voids in the sidewalls or other imperfections and irregularities of the layers after the manufacturing process. As a reference, the weights of the soft lattice structures were recorded after 3D printing and compared with the theoretical values. These data were used to quantitatively analyze any differences between the printed samples and corroborate the qualitative evaluations of the printing quality (Figure S4). The numerical results approximately coincided with the experimental data, and the coefficient of variation (COV) of this latter was 0.87%, 3.12%, and 2.54% for honeycomb, schwartz-P, and gyroid structures, respectively. To seek accuracy, since the experimental weights of the gyroid lattices were slightly lower than the theoretical values, the structures were analyzed through optical microscopy. The external surfaces did not show defects or irregularities, so the lattices were cut in half with a scalpel (to not alter the 3D printed layers) to evaluate the internal parts: some "micrometric cavitations" emerged with an average value of 380 μm (Figures S5). These voids could lead to a decrease in the structure's overall weight but can also result in a reduction of mechanical behavior (no micrometric cavitations were identified in the honeycomb and schwartz-P structures, Figure S5). These data were also confirmed by SEM analysis (Figures 2D). The 3D printed honeycomb and schwartz-P structures did not exhibit defects such as sagging, improper layer adhesion or porosity (Figure S6A-B). On the contrary, microscopic pores were instead present in the gyroid structures (Figure S6C), which might adversely affect the mechanical performance of the TPU-based structures. Unfortunately, this factor goes beyond the accuracy of the design and the fine-tuning of the printing parameters, but must be considered for specific applications.

Nevertheless, good reproducibility of the specimens was obtained. Such results emphasize the efficiency and potential scalability of the FFF process to produce controlled soft lattice structures with different unit cell sizes, lattice types, scales, and associated parameters.

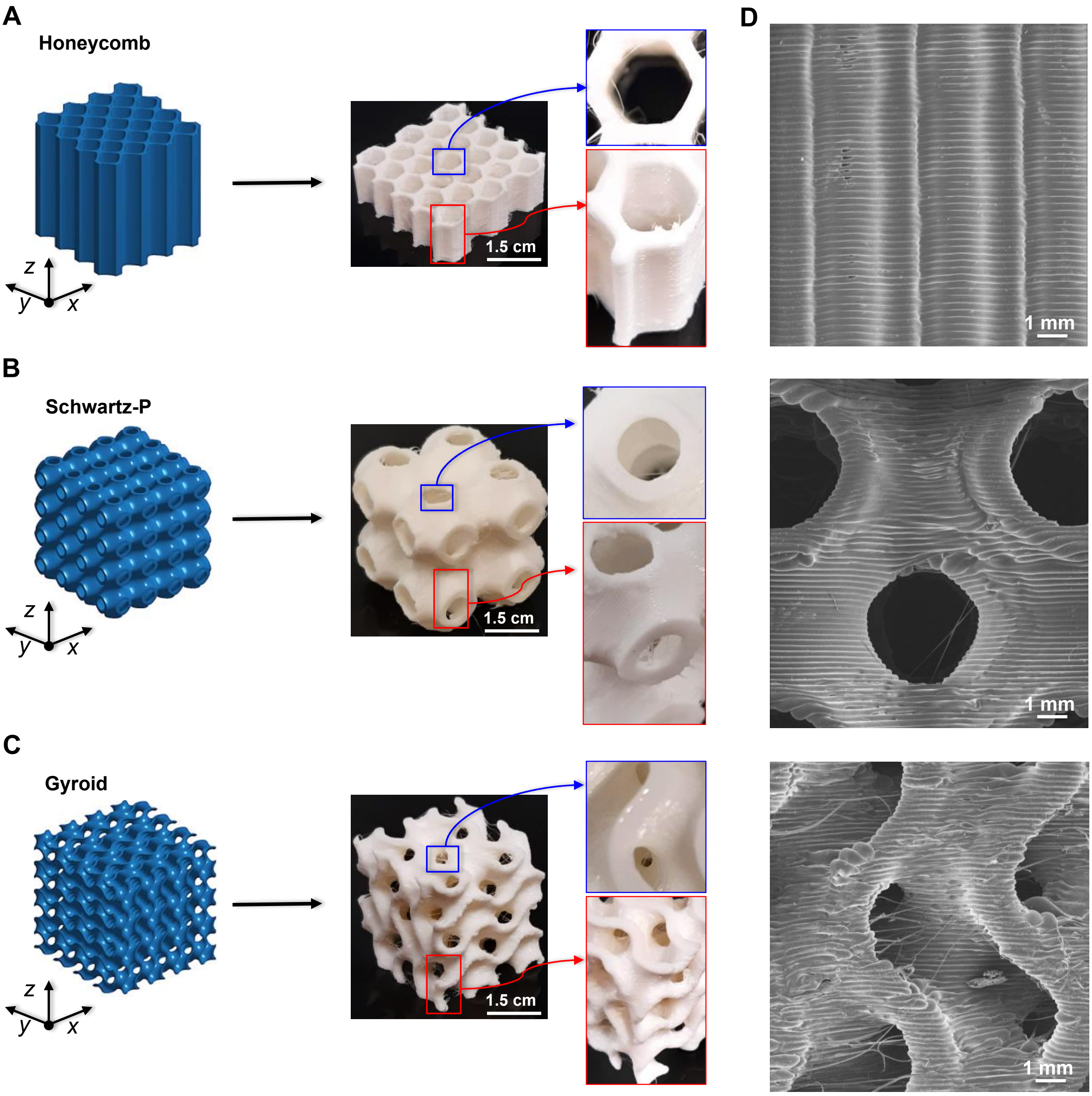

Figure 2. FLatt Pack design matrix lattices and corresponding 3D-printed (A) honeycomb, (B) schwartz-P, and (C) gyroid matrix soft scaffolds built with the TPU filament. The magnification of the upper surface (in blue) and sidewalls (in red) shows the printing quality of all soft lattices without any visible voids, imperfections, or irregularities after the manufacturing process. (D) SEM images of the TPU-based lattice structures. No visible defects, sagging, and improper layer adhesion are observed in all honeycomb and schwartz-P specimens. Microscopic pores are present in the gyroid structures.

3.2. FEA simulations of compressive behavior for the TPMS and honeycomb soft structures

To gain insights into the mechanical behavior of each designed structure, we used both FLatt Pack – Relative Modulus Estimation and FE models. Using FLatt Pack it was possible to explore the relative elastic modulus against volume fraction for selected cell types along the *x*, *y*, and *z* directions [52, 53]. This information allows one to select the cell type, volume fraction, and orientation most suitable for the intended application, and have a preliminary and dimensionless estimate of the behavior of the structure before the use of FE analysis. We noticed how stiffness increases for all tested structures by increasing the volume fraction (Figure 3 A-C). In contrast, the relative elastic modulus tends to reach a plateau below the 0.2 volume fraction (equal to a unit cell size of 6 mm), confirmed by other previous studies [54, 55]. However, while for the schwartz-P and gyroid structures the relative modulus appeared similar in the *x*, *y*, and *z* directions with an exponential increment, it was not so for the honeycomb structures. The latter displayed an exponential increase in the *x* and *y* directions with small variations of relative modulus values, while in the *z* direction, it was possible to observe a linear increase with high values of the relative modulus. This increase is due to the orientation of the vertical walls of the honeycomb structure, which contributes to the model's overall rigidity and makes the honeycomb topology, along this direction, a stretching-dominated structure [56].

Next, we examined this behavior on all structures using linear FE analysis. Using the FE simulation, the amount of applied force was obtained, and the equivalent compressive elastic modulus was then calculated as the ratio of compressive stress to compressive strain in the *x*, *y*, and *z* direction of interest (see Equation (6)). The obtained elastic moduli showed the variability of the mechanical properties of each lattice with the unit cell sizes along the *x*, *y*, and *z* directions (Figure 3 D-F). These results agree with the dimensionless data obtained through the FLatt Pack software. The different structures were expected to have a wide range of direction-dependent compressive elastic moduli (Table 2), controlled by the design parameters such as cell type, the surface-to-volume fraction, and the length of the periodic minimal surfaces. The distribution of von Mises stress for comparing honeycomb, schwartz-P, and gyroid structures is shown in Figure 4.

Honeycomb				Schwartz-P				Gyroid			
Unit cell size (mm)	E_x (MPa)	E_y (MPa)	E_z (MPa)	Unit cell size (mm)	E_x (MPa)	E_y (MPa)	E_z (MPa)	Unit cell size (mm)	E_x (MPa)	E_y (MPa)	E_z (MPa)
3	7.53	7.18	18.49	6	1.98	1.98	1.98	6	5.86	5.80	5.93
4	4.06	3.96	14.36	8	1.11	1.11	1.11	8	3.75	3.70	3.72
5	2.36	2.35	11.51	10	0.78	0.78	0.78	10	2.72	2.65	2.68
6	1.53	1.49	7.99	12	0.56	0.56	0.56	12	2.03	1.98	2.03

Table 2. Comparison of compressive elastic moduli in the *x*, *y*, and *z* directions obtained from the FE linear model of honeycomb, schwartz-P, and gyroid matrix soft lattice scaffolds with different unit cell sizes.

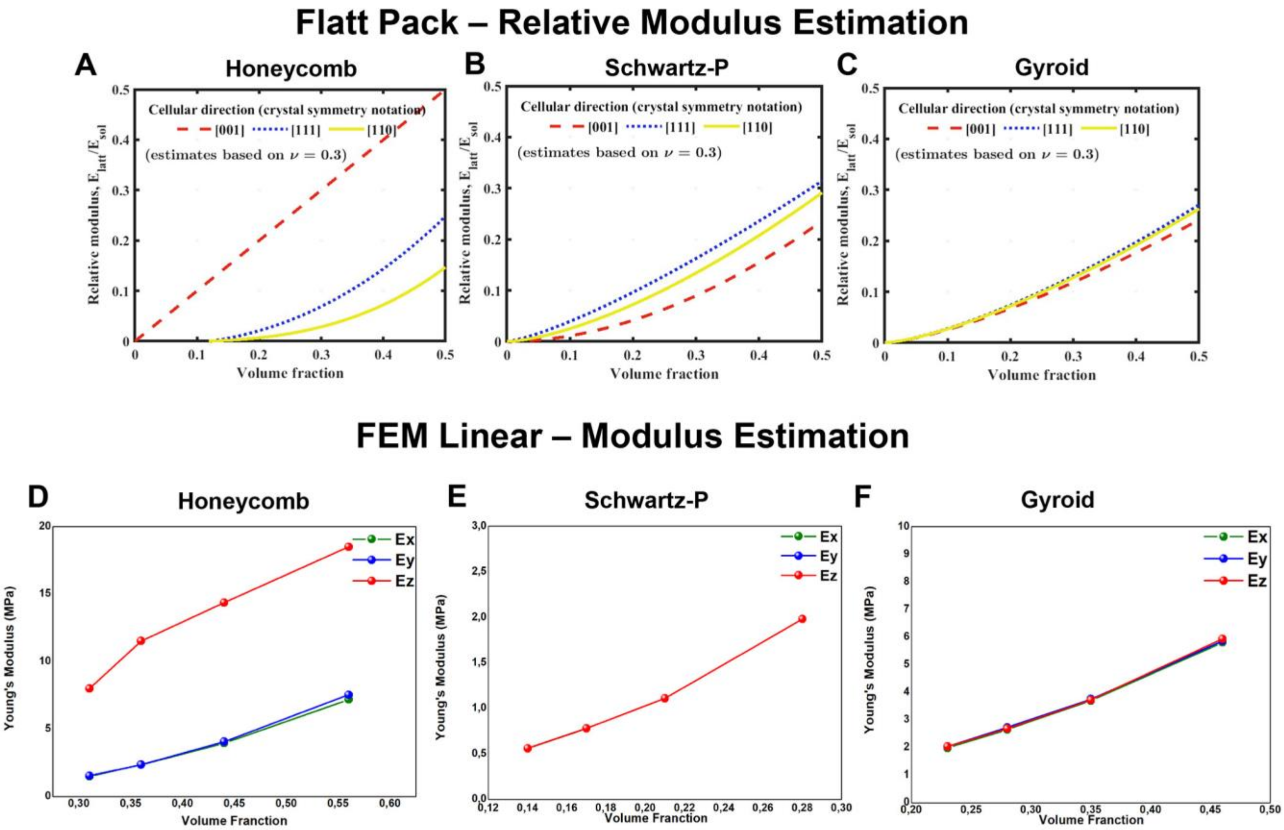

Figure 3. Comparison of (A-C) FLatt Pack – Relative Modulus Estimation and (D-F) linear FE models to explore the elastic modulus against volume fraction for selected cell type along the *x*, *y*, and *z* directions. In (E) all curves perfectly overlap.

In detail, the analysis of the honeycomb structures confirmed that Young's moduli in the *x* and *y* directions have the same value, with minor variations probably related to the cells repetition, characterized by half the original thickness at the upper and lower parts of the scaffold when creating the 3D model. Instead, as expected, the Young's moduli in the *z* direction (i.e., out-of-plane direction) showed values 10-fold higher than those for the in-plane moduli. The out-of-plane direction results were always stiffer than in-plane directions due to the orientation of the vertical walls, which contribute to the overall stiffness of the model (Figure 4 A). Conversely, we observed that the values of Young's moduli for schwartz-P and gyroid structures have no directional dependence, probably due to the symmetry in their geometries (Figure 4 B-C). Also, the increase in the unit cell size, maintaining the same thickness of the model, led to a decrease in the volume fraction and consequently a reduction in the value of the compressive modulus.

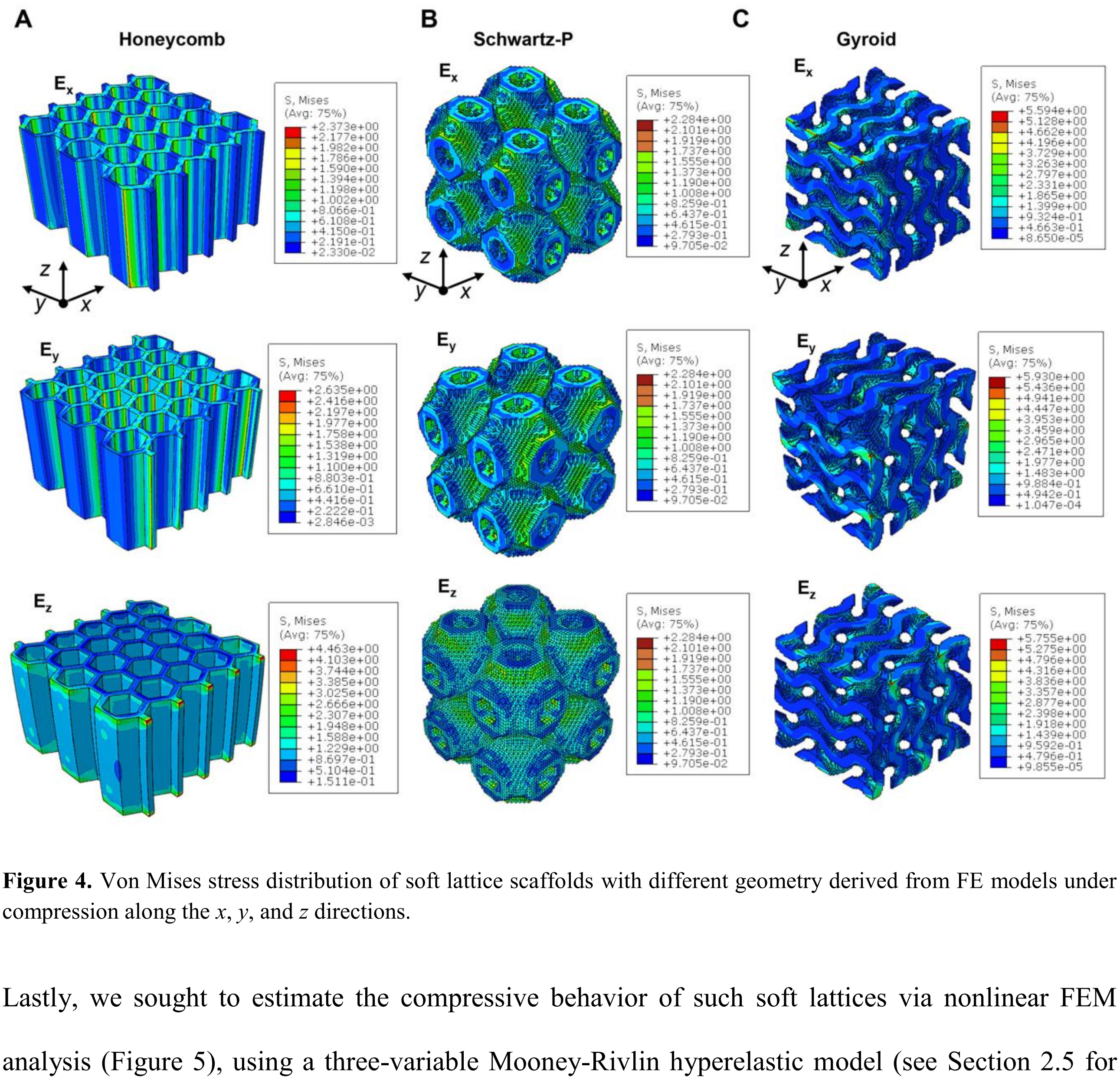

Figure 4. Von Mises stress distribution of soft lattice scaffolds with different geometry derived from FE models under compression along the *x*, *y*, and *z* directions.

Lastly, we sought to estimate the compressive behavior of such soft lattices via nonlinear FEM analysis (Figure 5), using a three-variable Mooney-Rivlin hyperelastic model (see Section 2.5 for further details), as this model would better describe the material behavior of TPU filament. The results showed an overall decrease in the compressive modulus of each tested structure compared to linear results; in particular a reduction of 23% is registered for schwartz-P and gyroid structure, among all unit cell sizes. This was not applicable for honeycomb structures, where differences in compressive modulus tend to be smaller as the unit cell size increases (it goes from 20% for the unit cell size of 3 mm, to 13% for the unit cell size of 6 mm). Additionally, based on the hyperelastic model, the honeycomb structures were stiffer than the schwartz-P and gyroid structure (Table S2).

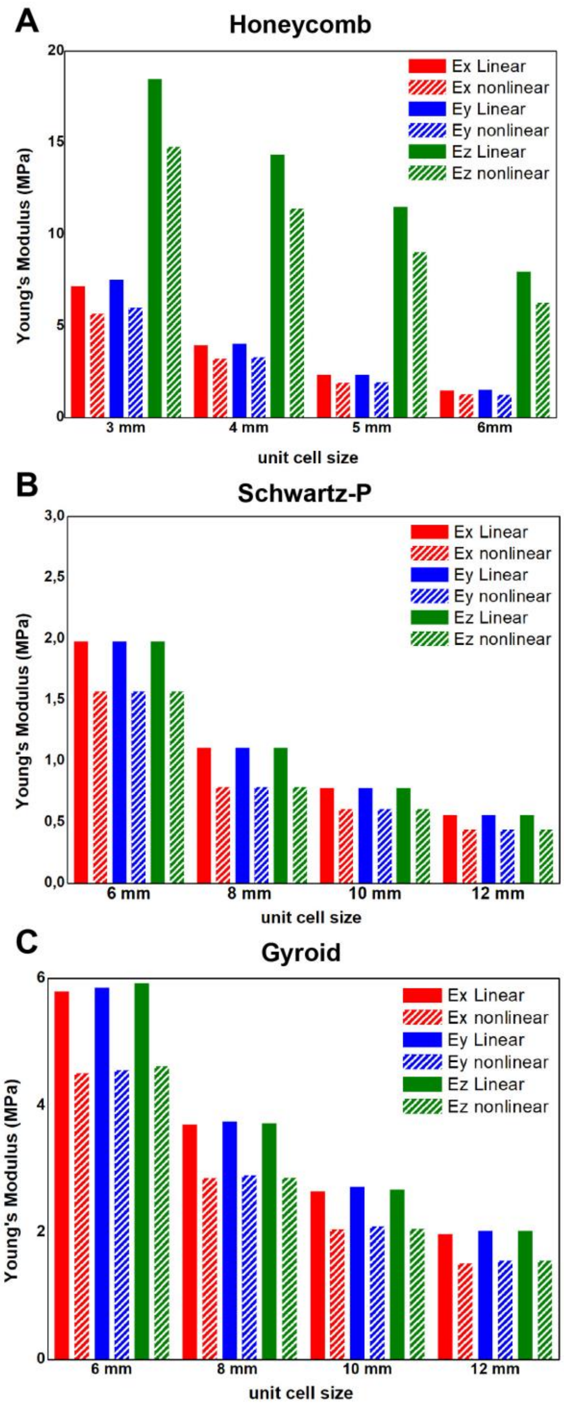

Figure 5. Comparison of linear (striped columns) and hyperelastic (full columns) FEM-derived compressive moduli along the *x*, *y*, and *z* directions of (A) honeycomb, (B) schwartz-P, and (C) gyroid matrix soft lattice scaffolds with different unit cell sizes.

These results may provide the basis for implementing a non-dimensional and dimensional data coupling-based approach for boosting the understanding of soft lattices in additive manufacturing design. Although theoretical, this approach can provide a deeper understanding of the structure-mechanical property relationship of each cell family that can be used to design soft innovative-engineered materials models with tunable properties. However, we must emphasize that the comparison between FE simulations and the additively manufactured structures may differ. Due to the intrinsic nature of the 3D printing process, the structure is generated via superimposition of subsequent layers, while the FE model is characterized as a continuous homogeneous solid with isotropic features. Hence, the influence of the layer bonding is not considered in the FE model, thus leading to be a key deviation to which attention must be paid when comparing theoretical versus experimental behaviors of 3D-printed structures.

3.3. Experimental results for the homogeneous soft structures

The results of the quasi-static compression tests are summarized in Figures 6 A-C, for the honeycomb, schwartz-P, and gyroid structures, respectively. The moduli were calculated based on Equation (6). For the sake of clarity, the theoretical modulus referred to the testing direction and obtained from the numerical analyses is provided. This value is the E_y (Table 2).

The honeycomb samples confirm what was obtained from the numerical analyses. These samples are characterized by a mass gain (Figure S4), which increases the E_y value. The only exception is the structure with a unit cell size of 3 mm, which, despite the mass increase (Figure S4), has an E_y value slightly lower (6.6±0.52 MPa) than the theoretical one (7.18 MPa). This behavior could be due to some minor irregularities on the printing walls.

For the schwartz-P, despite the increase in mass, which characterizes the 3D printed samples, we recorded an E_y value consistently lower than the numerical values. The mass gain is due to the change in the extrusion multiplier parameter set to 1.1 to guarantee the printability of the structure. Only when this mass increase significantly overcomes the theoretical value (i.e., in the lattice with a unit cell size of 12 mm, Figure S4), there is an opposite situation among theoretical and numerical values. This difference is due to the mesh used for simulating the behavior of the schwartz-P structures. As shown in Figure 4, the selected mesh tends to overestimate the dimensions of the structure, especially on the sloped surfaces. For the 12 mm unit cell size structure, this overestimation almost compensates the increase in the mass value, probably because there is a larger volume fraction and therefore more finite elements in proportion. The mass gain is less evident in the case of 6 mm unit cell because the printing path leaves material gaps at the bridges, which connect the unit cells (Figure S7). This issue does not occur in the other samples schwartz-P samples (Figure S7).

Finally, the gyroid demonstrated the highest discrepancy between theoretical and experimental values for all the tested sizes (Figure 6C). An experimental modulus lower than the theoretical one was expected considering the mass deficit, which characterizes these samples (Figure S4), as also demonstrated by the presence of micrometric cavitations (Figure S5) and the material gaps which are present at the connection zones (i.e., the bridges) of unit cells in the case of scaffolds of 6 mm unit cell dimension (Figure S7). Indeed, the influence of the mass deficit on the mechanical behavior of the structures is even more evident in the structure having a 6 mm unit cell size. This structure has the highest volume fraction (i.e., 0.46, Table 1), and it is also bending-dominated, as demonstrated by Maskery et al., [57]. Hence, the scaling-law that describes the influence of the volume fraction on the relative elastic modulus (i.e., the modulus of the lattice divided by the modulus of the material it is made from) has a coefficient equal to 2 [56], which means that especially at high-volume fractions, the relative modulus of the structure is more sensitive to volume-fraction changes.

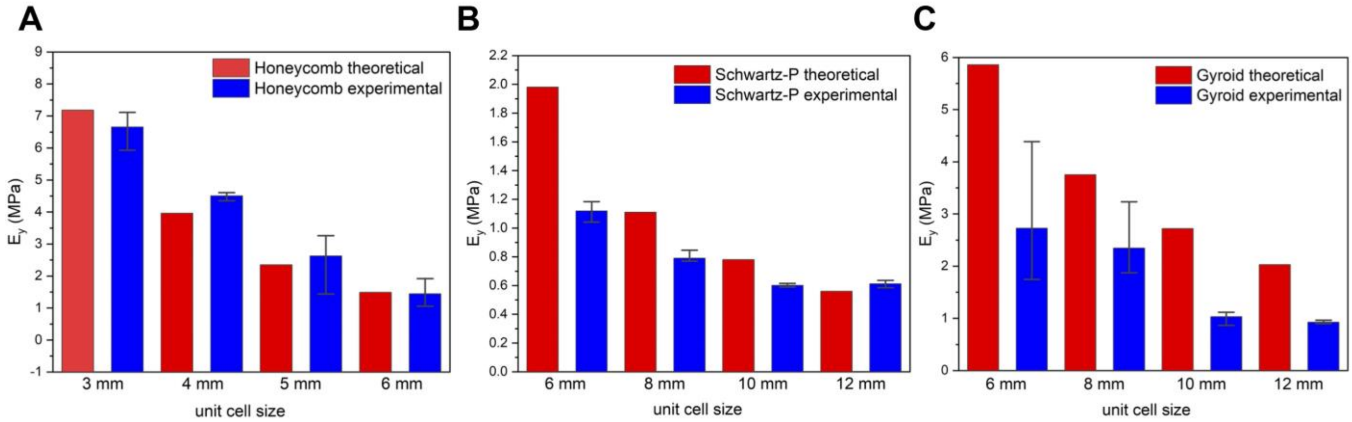

Figure 6. Comparison among theoretical and experimental Young's Moduli of the analyzed structure: (A) honeycomb, (B) schwartz-P, and (C) gyroid. According to the selected testing direction, the theoretical values are the E_y provided in Table 2.

3.4. Graded and hybrid soft structures

Lastly, we explore two further possibilities of lattice structure design using the optimized print parameters: the gyroid volume fraction grading and the honeycomb hybridization. Both can provide novel soft lattice behavior, such as layer-by-layer structural collapse and tailorable impactor deceleration under dynamic loading. Once designed, the honeycomb three-layered hybrid structure (see section 2.3) was 3D printed using the optimized process parameters for a unit cell of 6 mm (Figure 7A, and Table S1). Then, we examined its compressive behavior using linear FEM analysis imposing a vertical displacement of the upper part equal to 40% of the model height and an encaster constraint in the lower part (see Section 2.5 for further details). The FEM deformation of the three-layer hybrid honeycomb lattice under compressive loading with the corresponding force-displacement curve is shown in Figure 7B. At low strain, all of the observed deformations were in the low-stiffness *x* direction regions, and the initial elastic response and plastic plateau are identified as (a) and (b) on the force-displacement curve. At the phase identified as (c), the cell walls were completing their bending into the stiffer configuration, reaching above (d) an extremely stiff configuration as the *x* regions at the bottom and top of the structure entered densification. The densification mechanism exists for all cellular structures at high strain, but in this case, it was localized to the *x* regions only. Finally, the three-layer hybrid lattice underwent a further increase in stiffness (e) as the compressive load was transferred solely through the remaining high-stiffness region *z* direction. The experimental force-displacement curve (Figure 7B) confirms the trend obtained through the numerical analysis, as demonstrated by the sample images at different test phases. However, there is a general overestimation of the force values: it might be due to the applied boundaries conditions, which lead to over constraining the overall structure.

In addition, it should be noted that the FE analysis conducted on the hybrid structure takes into account some approximations in order to allow the convergence of the simulation (see section 2.5); however, we do not exclude that in future studies it will be possible to apply the advanced material model aimed at studying the hysteretic behavior of the hyperelastic TPU polymer bioinspired by the morphology of the sea urchin for complex soft hybrid structures, as recently reported in [58].

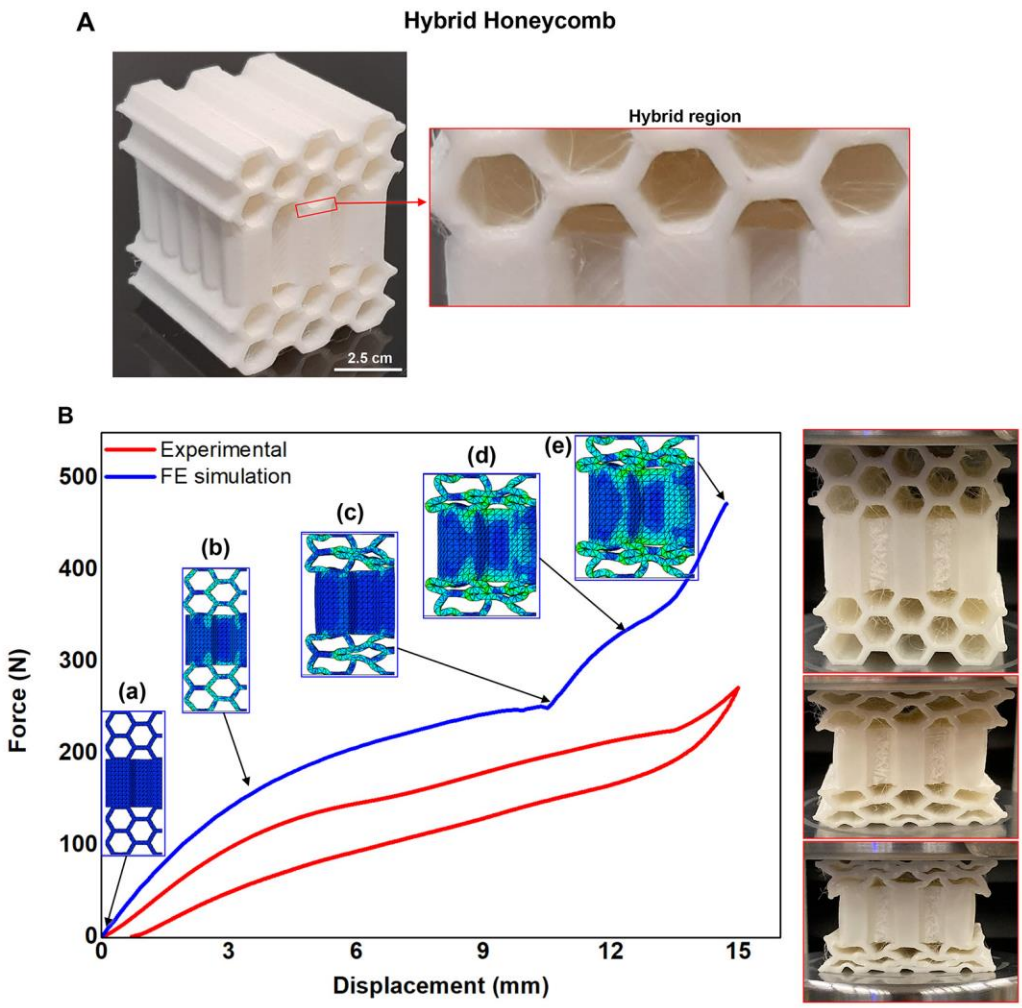

Figure 7. (A) 3D printed three-layer hybrid honeycomb soft lattice. In red magnification of the hybrid region, which shows how the two regions are well joined together with no visible voids. (B) Numerical and experimental force-displacement curves of the three-layer hybrid honeycomb lattice under compressive loading, which show: (a) initial elastic response and (b) plastic plateau of the hybrid soft lattice; (c) bending phase of cell walls; (d) stiffer configuration as the regions at the bottom and top of the structure entered densification; (e) further increase in stiffness as the compressive load transfers solely through the remaining high-stiffness region (i.e., in the *z*-direction). On the left, a sequence of photos taken during the experimental tests at different compression stages.

The soft gyroid graded lattice was generated using FLatt Pack, by selecting a linear gradient variation of the volume fraction from 0.23 to 0.46 (corresponding to a thickness variation from 1 mm to 2 mm). A 2 × 2 × 2 lattice was generated for the FE simulations (Figure 8 A-B) and 3D printed using optimized parameters (Figure 8C, and Table S1). The compression simulation was performed with the imposed displacement oriented as the direction selected for increasing the thickness. The corresponding force-displacement curve was compared with the curves of the structures having a uniform thickness of 1 mm and 2 mm (Figure 8D), respectively. FE simulations displayed that in the displacement region analyzed, the soft gyroid graded lattice had an intermediate behavior compared to those with a uniform thickness of 1 mm and 2 mm. However, it was impossible to go beyond a 1 mm displacement due to computational limits. This would have allowed evaluating whether cell walls between 1 and 1.5 mm completed their folding in the most rigid configuration and entered densification, then undergoing a further increase in stiffness due to the remaining 2 mm thick region. This computational bottleneck was overcome by testing the 3D-printed sample. As shown in Figure 8E and specifically in the zoomed image, the value of the force at 1 mm displacement (90 N) is similar to the theoretical one (95 N). As expected, the increase in the structure's stiffness is instead shown on the left of Figure 8E. There is a monotonic increase in the stiffness until the densification phase is reached. The bottom of Figure 8E shows the sample at different compression stages.

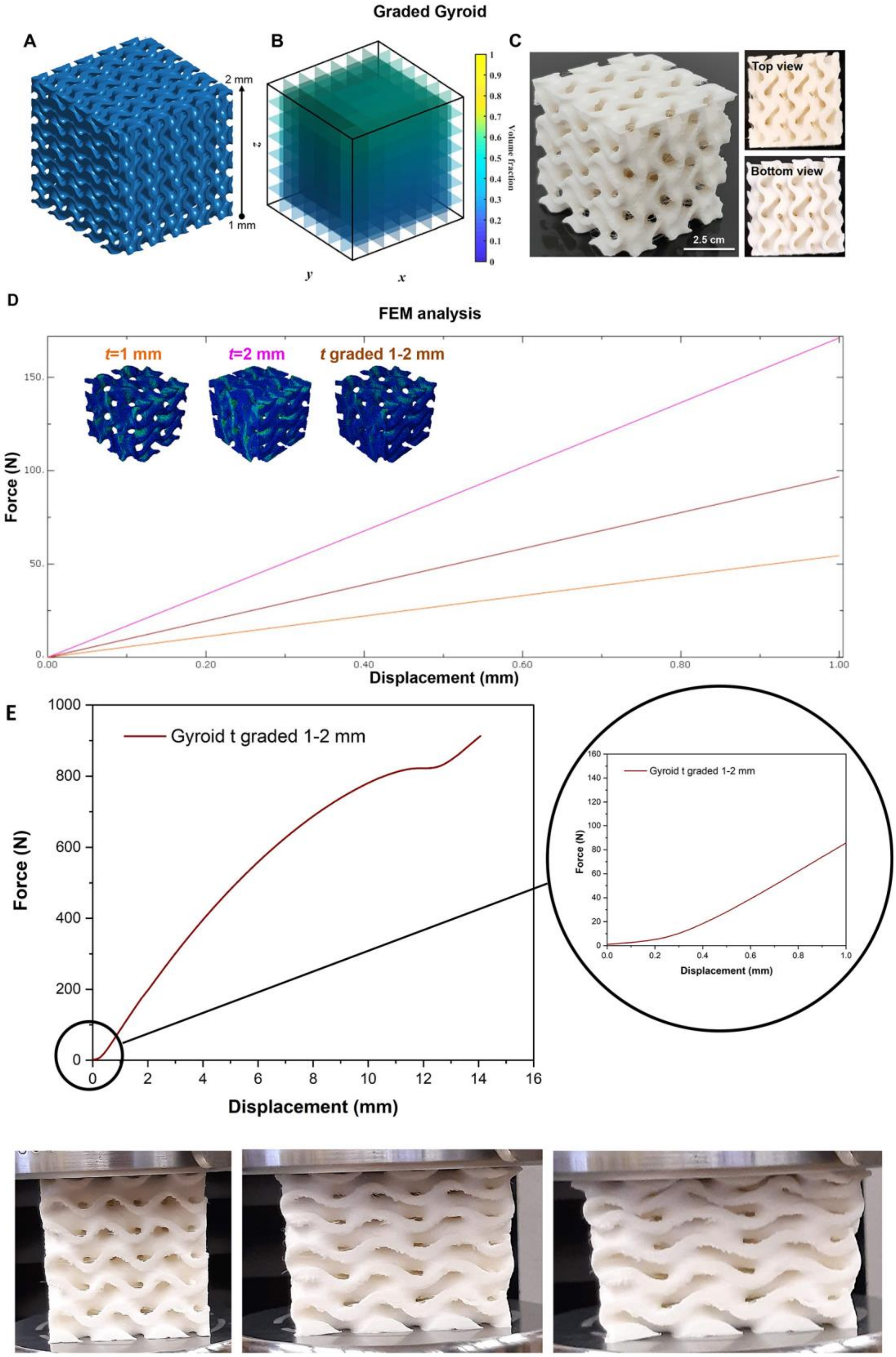

Figure 8. (A) Matrix representation of soft graded gyroid lattice, (B) and corresponding linear volume fraction preview. (C) Soft graded gyroid printed sample. (D) Force-displacement curve derived from FEM deformation of the soft graded gyroid lattice (in brown) under compressive loading, compared with lattices with a uniform thickness of 1 mm (in orange) and 2 mm (in magenta). (E) The experimental force-displacement curve and a magnification of the same chart from 0 to 1 mm of displacement. At the bottom is the sample during different compression stages.

4. Conclusion

The study describes the numerical and experimental analyses performed to explore the behavior of a selection of lattices, such as the honeycomb, the schwartz-P, and the gyroid 3D-printed using thermoplastic polyurethane (TPU) as feedstock material. These soft lattices can be relevant for multiple purposes, especially in the biomedical field. They could be used to develop biological scaffolds, biomedical implants, porous structures for 3D cell culture, soft orthosis, and soft cushions to control pressure ulcers or bedsores in patients with immobility who are forced to use a wheelchair. They could also be used in all circumstances where there is semi-permanent contact with the skin, such as lower limb prostheses or masks for non-invasive ventilation (NIV) for severe acute respiratory syndrome coronavirus (SARS-CoV) or neuromuscular patients. However, despite this wide range of possible applications, there are still not enough studies exploring their behavior and technical feasibility concerning printing-related issues. This paper overcomes this gap by proposing a collection of design and printing guidelines for fabricating these structures using the fused filament fabrication (FFF) process. The selection of this printing process was made on purpose, considering its wide diffusion and flexibility in terms of materials that could be potentially 3D-printed, for example, combining the thermoplastic matrix with specific additives tailored for the biomedical application of interest. Multiple design and printing parameters were explored. We started defining the main design variables for the scaffolds, such as the cell type, the unit cell size, and the volume fraction. These variables were combined with the selected printing parameters to be tuned to obtain self-supporting, stable structures and repeatable printing results.

In particular, we optimized the multi-scale printing parameters, noting that for the honeycomb structure with a unit cell size of 3 mm, to achieve a good surface quality of the structure without debris and lumps of filaments, an extrusion width of 0.65 mm, a retraction distance of 1 mm, a retraction speed of 2,400 mm/min, and a printing speed of 1,100 mm/min must be applied. On the other hand, for unit cells from 4 mm up to over 6 mm, the same process parameters as the 3 mm unit cell size could be used, but with a print speed of up to 3,000 mm/min. Instead, for the TMPS schwartz-P and gyroid structures with a smaller unit cell of 6 mm, the same printing parameters can be applied, namely: a retraction speed of 3,000 mm/min to avoid debris on the surface of the structure and a printing speed of 1,000 mm/min; with the increase of the unit cell size it was possible to increase the printing speed up to 2,400 mm/min to obtain the same result in terms of surface quality of the gratings. However, unlike the gyroid structures, for the schwartz-P structures it was necessary to use the extrusion multiplier when creating the cantilevered cell walls.

In parallel, numerical analyses were performed to understand the scaffolds' behavior with the selected design parameters in linear and hyperelastic conditions, to explore which model would better describe the material behavior of TPU filament. These analyses were validated experimentally using quasi-static compression tests, which showed a good matching with the theoretical data. Together with homogenous samples, i.e., scaffolds having a constant thickness, we also successfully explored the effectiveness of the optimized printing parameters in case of a not-constant thickness (i.e., graded) and hybrid structures.

The obtained results are promising, but further research efforts are needed to extend more and more research opportunities in the design and printing of soft lattices, considering the wide range of applications in which they could be employed.

Declaration of Competing Interest

The authors declare no competing interest.

Author Contributions: "Conceptualization, R.P.; methodology, R.S., S.G., and R.P.; software, R.S., and R.P.; validation, R.S., S.G., and R.P.; formal analysis, R.S. and R.P.; investigation, R.S., S.G., and R.P.; data curation, R.S. and R.P.; writing—original draft preparation, S.G., and R.P.; writing—review and editing, R.S., S.G., S.R., and R.P.; visualization, R.S., S.G., S.R., and R.P.; supervision, R.P.; project administration, R.P.; funding acquisition, S.R. and R.P.. All authors have read and agreed to the published version of the manuscript."

Acknowledgments: We are grateful to Rotary Club Milano Linate for the financial support on 3D printing technology. We thank Treed Filaments for providing Thermoplastic polyurethane (TPU) filaments and for helpful discussions on the printing properties.

References

[1] M. Martorelli, A. Gloria, C. Bignardi, M. Cali, S. Maietta, Design of Additively Manufactured Lattice Structures for Biomedical Applications, J Healthc Eng 2020 (2020) 2707560.
[2] C. Chatzigeorgiou, B. Piotrowski, Y. Chemisky, P. Laheurte, F. Meraghni, Numerical investigation of the effective mechanical properties and local stress distributions of TPMS-based and strut-based lattices for biomedical applications, J Mech Behav Biomed Mater 126 (2021) 105025.
[3] W. Chen, J. Yang, H. Kong, M. Helou, D. Zhang, J. Zhao, W. Jia, Q. Liu, P. He, X. Li, Fatigue behaviour and biocompatibility of additively manufactured bioactive tantalum graded lattice structures for load-bearing orthopaedic applications, Mater Sci Eng C Mater Biol Appl 130 (2021) 112461.
[4] S. Dhiman, M. Singh, S.S. Sidhu, M. Bahraminasab, D.Y. Pimenov, T. Mikolajczyk, Cubic Lattice Structures of Ti6Al4V under Compressive Loading: Towards Assessing the Performance for Hard Tissue Implants Alternative, Materials (Basel) 14(14) (2021).
[5] F.N. Mullaveettil, R. Dauksevicius, Y. Wakjira, Strength and elastic properties of 3D printed PVDF-based parts for lightweight biomedical applications, J Mech Behav Biomed Mater 120 (2021) 104603.
[6] A.I.H. Nasrullah, S. Puji Santosa, D. Widagdo, F. Arifurrahman, Structural Lattice Topology and Material Optimization for Battery Protection in Electric Vehicles Subjected to Ground Impact Using Artificial Neural Networks and Genetic Algorithms, Materials (Basel) 14(24) (2021).
[7] Del Olmo E., Grande E., Samartin C.R., Bezdenejnykh M., Torres J., Blanco N., Frovel M., C. J., Lattice Structures For Aerospace Applications, Proceedings of the 12th European Conference on Spacecraft Structures, Materials and Environmental Testing, 2012.
[8] Büşra Aslan, A.R. Yıldız, Optimum design of automobile components using lattice structures for additive manufacturing, Materials Testing 62(6) (2021).
[9] R. Sala , S. Regondi, R. Pugliese., Design Data and Finite Element Analysis of 3D Printed Poly(ε-Caprolactone)-Based Lattice Scaffolds: Influence of Type of Unit Cell, Porosity, and Nozzle Diameter on the Mechanical Behavior, Eng 3(1) (2022) 9-23.
[10] Q. Chen, N.M. Pugno, Bio-mimetic mechanisms of natural hierarchical materials: a review, J Mech Behav Biomed Mater 19 (2013) 3-33.
[11] L.J. Bonderer, A.R. Studart, L.J. Gauckler, Bioinspired design and assembly of platelet reinforced polymer films, Science 319(5866) (2008) 1069-73.
[12] S. Zhang, Fabrication of novel biomaterials through molecular self-assembly, Nat Biotechnol 21(10) (2003) 1171-8.
[13] S.M. Sajadi, P.S. Owuor, S. Schara, C.F. Woellner, V. Rodrigues, R. Vajtai, J. Lou, D.S. Galvao, C.S. Tiwary, P.M. Ajayan, Multiscale Geometric Design Principles Applied to 3D Printed Schwarzites, Adv Mater 30(1) (2018).

[14] I. Maskerya, A.O. Aremu, L. Parry, R.D. Wildman, C.J. Tuck, I.A. Ashcroft, Effective design and simulation of surface-based lattice structures featuring volume fraction and cell type grading, Materials and Design 155(5) (2018) 220-232.
[15] I. Maskery, L. Sturm, A.O. Aremu, A. Panesar, C.B. Williams, C.J. Tuck, R.D. Wildman, I.A. Ashcroft, R.J.M. Hague, Insights into the mechanical properties of several triply periodic minimal surface lattice structures made by polymer additive manufacturing, Polymer 152 (2018) 62-71.
[16] Chen Pan, Yafeng Han, J. Lu, Design and Optimization of Lattice Structures: A Review, Appl. Sci. 10(18) (2020).
[17] X. Zhang, Y. Wang, B. Ding, X. Li, Design, Fabrication, and Mechanics of 3D Micro-/Nanolattices, Small 16(15) (2020) e1902842.
[18] Mark Helou, S. Kara, Design, analysis and manufacturing of lattice structures: an overview, International Journal of Computer Integrated Manufacturing 31(3) (2017) 243-261.
[19] Christiane Beyer, D. Figueroa, Design and Analysis of Lattice Structures for Additive Manufacturing, J. Manuf. Sci. Eng. 138(12) (2016).
[20] Shanqing Xu, Jianhu Shen, Shiwei Zhou, Xiaodong Huang, Y.M. Xie, Design of lattice structures with controlled anisotropy, Materials and Design 93(5) (2016).
[21] Tino Stanković, Jochen Mueller, Paul Egan, K. Shea, A Generalized Optimality Criteria Method for Optimization of Additively Manufactured Multimaterial Lattice Structures, J. Mech. Des. 137(11) (2015).
[22] Pugliese R., Beltrami B., Regondi S., Lunetta C., Polymeric biomaterials for 3D printing in medicine: An overview, Annals of 3D Printed Medicine 2(1) (2021).
[23] Mohammad Qasim Shaikh, Serena Graziosi, S.V. Atre, Supportless printing of lattice structures by metal fused filament fabrication (MF3) of Ti-6Al-4V: design and analysis, Rapid Prototyping Journal 27(7) (2021).
[24] M.Jamshidian, N.Boddeti, D.W.Rosen, O.Weeger, Multiscale modelling of soft lattice metamaterials: Micromechanical nonlinear buckling analysis, experimental verification, and macroscale constitutive behaviour, International Journal of Mechanical Sciences 188 (2020).
[25] Xiaowei Zhu, Yanqiu Chen, Yu Liu, Yongqiang Deng, Changyu Tang, Weilian Gao, Jun Mei, Junhua Zhao, Tong Liu, J. Yang, Additive manufacturing of elastomeric foam with cell unit design for broadening compressive stress plateau, Rapid Prototyping Journal 24(9) (2018).
[26] David W. Holmes, Dilpreet Singh, Riki Lamont, Ryan Daley, David P. Forrestal, Peter Slattery, Edmund Pickering, Naomi C. Paxton, Sean K. Powell, M.A. Woodruff, Mechanical behaviour of flexible 3D printed gyroid structures as a tuneable replacement for soft padding foam, Additive Manufacturing 50 (2022).
[27] H.M.A. Kolken, S.J.P. Callens, M.A. Leeflang, M.J. Mirzaali, A.A. Zadpoor, Merging strut-based and minimal surface meta-biomaterials: decoupling surface area from mechanical properties, Additive Manufacturing (2022).
[28] Elliot S. Bishop, Sami Mostafa, Mikhail Pakvasa, Hue H. Luu, Michael J. Lee, Jennifer Moriatis Wolf, Guillermo A. Ameer, Tong-Chuan He, R.R. Reid, 3-D bioprinting technologies in tissue engineering and regenerative medicine: Current and future trends, Genes & Diseases 4(4) (2017).
[29] Fabrizio Fina, Alvaro Goyanes, Christine M.Madla, Atheer Awad, Sarah J.Trenfield, Jia Min Kuek, Pavanesh Patel, Simon Gaisford, A. W.Basit, 3D printing of drug-loaded gyroid lattices using selective laser sintering, International Journal of Pharmaceutics 547(2) (2018).
[30] Roland K.Chen, Yu-an Jin, Jeffrey Wensman, AlbertShih, Additive manufacturing of custom orthoses and prostheses—A review, Additive Manufacturing 12 (2016).
[31] Maskery I., A. I.A., The deformation and elastic anisotropy of a new gyroid-based honeycomb made by laser sintering, Additive Manufacturing 36 (2020).

[32] Nan Yang, Yifan Song, Jinlun Huang, Yuetao Chen, I. Maskery, Combinational design of heterogeneous lattices with hybrid region stiffness tuning for additive manufacturing, Materials and Design 209 (2021).
[33] Yingzhu Wang, Weiang Luo, Junwen Huang, Chaohua Peng, Hongchao Wang, Conghui Yuan, Guorong Chen, Birong Zeng, L. Dai, Simplification of Hyperelastic Constitutive Model and Finite Element Analysis of Thermoplastic Polyurethane Elastomers, Macromolecular Theory and Simulation 29(4) (2020).
[34] Francesco Tamburrino, Serena Graziosi, M. Bordegoni, The Design Process of Additively Manufactured Mesoscale Lattice Structures: A Review J. Comput. Inf. Sci. Eng. 18(4) (2018).
[35] F. Libonati, S. Graziosi, F. Ballo, M. Mognato, G. Sala, 3D-Printed Architected Materials Inspired by Cubic Bravais Lattices, ACS Biomater Sci Eng (2021).
[36] JánosPlocher, A. Panesar, Effect of density and unit cell size grading on the stiffness and energy absorption of short fibre-reinforced functionally graded lattice structures, Additive Manufacturing 33 (2020).
[37] Ajeet Kumar, Saurav Verma, J.-Y. Jen, Supportless Lattice Structures for Energy Absorption Fabricated by Fused Deposition Modeling, 3D Printing and Additive Manufacturing 7(2) (2020).
[38] Mayur Jiyalal Prajapati, Ajeet Kumar, Shang-ChihLin, Jeng-YwanJeng, Multi-material additive manufacturing with lightweight closed-cell foam-filled lattice structures for enhanced mechanical and functional properties, Additive Manufacturing 54 (2022).
[39] I. Maskery, L.A. Parry, D. Padr˜ao, R.J.M. Hague, I.A. Ashcroft, FLatt Pack: A research-focussed lattice design program, Additive Manufacturing 49 (2022).
[40] SuWang, Zhang'ao Shi, Linlin Liu, Zhili Huang, Zhong Li, Juncai Liu, Y. Hao, Honeycomb structure is promising for the repair of human bone defects, Materials and Design 207 (2021).
[41] Sing Ying Choy, Chen-Nan Sun, Kah Fai Leong, JunWei, Compressive properties of functionally graded lattice structures manufactured by selective laser melting, Materials and Design 131(5) (2017) 112-120.
[42] Ajit Panesar, Meisam Abdi, Duncan Hickman, I. Ashcroft, Strategies for functionally graded lattice structures derived using topology optimisation for Additive Manufacturing, Additive Manufacturing 19 (2018) 81-94.
[43] H.Niknam, A.H.Akbarzadeh, Graded lattice structures: Simultaneous enhancement in stiffness and energy absorption, Materials and Design 196 (2020).
[44] Chang Liu, Zongliang Du, Weisheng Zhang, Yichao Zhu, X. Guo, Additive Manufacturing-Oriented Design of Graded Lattice Structures Through Explicit Topology Optimization, J. Appl. Mech. 84(8) (2017).
[45] BingYi, YuqingZhou, Gil HoYoon, KazuhiroSaitou, Topology optimization of functionally-graded lattice structures with buckling constraints, Computer Methods in Applied Mechanics and Engineering 354(1) (2019) 593-619.
[46] C. Ursini, L. Collini, FDM Layering Deposition Effects on Mechanical Response of TPU Lattice Structures, Materials (Basel) 14(19) (2021).
[47] L. Rodriguez-Parada, S. de la Rosa, P.F. Mayuet, Influence of 3D-Printed TPU Properties for the Design of Elastic Products, Polymers (Basel) 13(15) (2021).
[48] Michael Robinson, Shwe Soe, Richard Johnston, Rhosslyn Adams, Benjamin Hanna, Roy Burek, Graham McShane, Rafael Celeghini, Marcilio Alves, P. Theobald, Mechanical characterisation of additively manufactured elastomeric structures for variable strain rate applications, Additive Manufacturing 27 (2019) 398-407.
[49] T. Reppel, K. Weinberg, Experimental Determination of Elastic and Rupture Properties of Printed Ninjaflex, TECHNISCHE MECHANIK 38(1) (2018) 104 – 112.

[50] I.Maskery, N.T.Aboulkhair, A.O.Aremu, C.J.Tuck, I.A.Ashcroft, Compressive failure modes and energy absorption in additively manufactured double gyroid lattices, Additive Manufacturing 16 (2017) 24-29.
[51] P. Platek, K. Rajkowski, K. Cieplak, M. Sarzynski, J. Malachowski, R. Wozniak, J. Janiszewski, Deformation Process of 3D Printed Structures Made from Flexible Material with Different Values of Relative Density, Polymers (Basel) 12(9) (2020).
[52] Guoying Dong, Yunlong Tang, Y.F. Zhao, A 149 Line Homogenization Code for Three-Dimensional Cellular Materials Written in matlab, J. Eng. Mater. Technol. 141(1) (2019).
[53] Zeyao Chen, Yi Min Xie, Xian Wu, Zhe Wang, Qing Li, S. Zhou, On hybrid cellular materials based on triply periodic minimal surfaces with extreme mechanical properties, Materials and Design 183 (2019).
[54] Sergio Ruiz de Galarreta, Jonathan R.T. Jeffers, S. Ghouse, A validated finite element analysis procedure for porous structures, Materials and Design 189 (2020).
[55] J. Kadkhodapour, H. Montazerian, A. Darabi, A.P. Anaraki, S.M. Ahmadi, A.A. Zadpoor, S. Schmauder, Failure mechanisms of additively manufactured porous biomaterials: Effects of porosity and type of unit cell, J Mech Behav Biomed Mater 50 (2015) 180-91.
[56] M.F. Ashby, The properties of foams and lattices, Philos Trans A Math Phys Eng Sci 364(1838) (2006) 15-30.
[57] I. Maskery, L. Sturm, A.O. Aremu, A. Panesar, C.B. Williams, R.D. C.J. Tuck, Wildman, I.A. Ashcroft, R.J.M. Hague, Insights into the mechanical properties of several triply periodic minimal surface lattice structures made by polymer additive manufacturing, Polymer 152 (2018) 62-71.
[58] A. Kumar, L. Collini, C. Ursini, J.-Y. Jeng, Energy Absorption and Stiffness of Thin and Thick-Walled Closed-Cell 3D-Printed Structures Fabricated from a Hyperelastic Soft Polymer, Materials (Basel) 15 (2022).

Supplementary information for

Insights into the printing parameters and characterization of thermoplastic polyurethane soft triply periodic minimal surface and honeycomb lattices for broadening material extrusion applicability

Riccardo Sala[1,‡], Stefano Regondi[1], Serena Graziosi[2,*], and Raffaele Pugliese[1,‡,*]

[1]NeMO Lab, ASST Niguarda Cà Granda Hospital, Milan, Italy.

[2]Department of Mechanical Engineering, Politecnico di Milano, Milan, Italy.

[‡]These authors contributed equally

[*]Corresponding author at: raffaele.pugliese@nemolab.it (R.P.), serena.graziosi@polimi.it (S.G.)

2.5. Finite element analysis

In the STEP section of the models, the option Nlgeom was set to "on" for allowing non-linearities in the models during compression simulations. The maximum number of increments was set to 100, with an increment size variable from an initial 0.01 up to 0.1. The minimum increment size was left to a default value of 1.0×10^{-5}. The output requested for such simulations were the stress distribution, the reaction forces, and the displacements of reference points selected and highlighted. The 3D eight-node linear isoparametric elements (C3D8H) were adopted for all models; no reduced integration was applied, but a hybrid formulation command was required due to the incompressibility of the simulated TPU. The average mesh size selected for this type of lattice was 0.25 mm, except for the 6 mm cell size where the average finite element size was set to 0.4 mm to avoid a too long computation time.

For the hybrid honeycomb in the STEP section, the non-linear geometry option was turned "on", and an initial increment of 0.01 was applied. Because of the complexity of the model, the minimum increment allowed was set to 1.0×10^{-9}. In the assembly section, the two planes were positioned on the top and the bottom of the model and constrained with the model using a TIE type constraint. Then, two different types of interactions were defined. One type considers the frictionless contact between the model and the two planes. The second one considers the self-contact among the surfaces in the honeycomb model to avoid auto intersection once compressed.

Then, the meshing procedure was conducted, selecting C3D10 quadratic tetrahedral elements with an average size of 0.7 mm. For the hyperelastic simulation, the element selected was C3D10H, where H stands for the hybrid formulation, enabling calculation with incompressible materials (i.e., D = 0). The two planes representative of the fixed and moving portion of the compressing machine were meshed with R3D4 quadrilateral elements, with an average mesh size of 4 mm (there was no need to use a finer mesh).

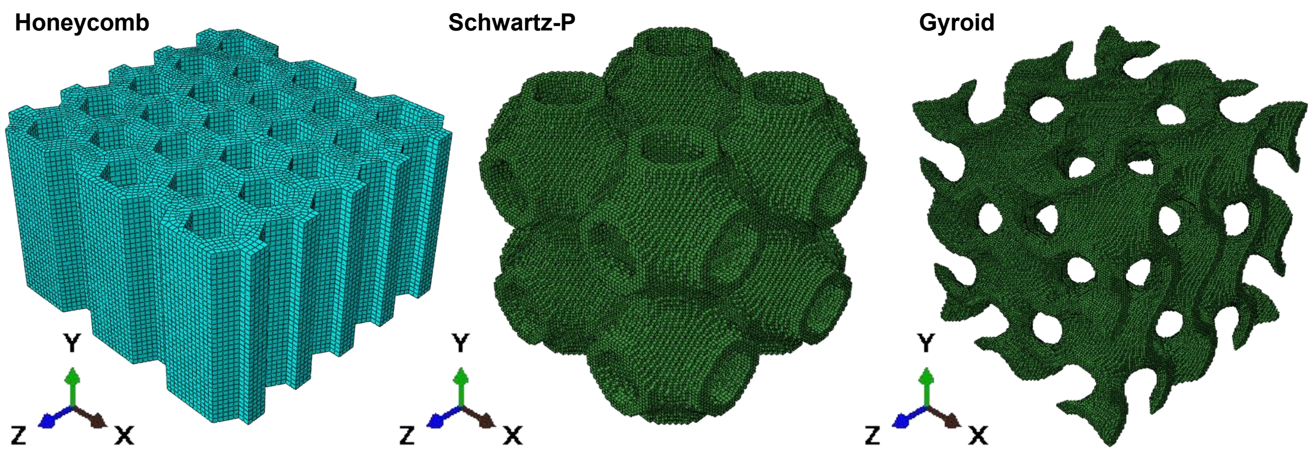

Figure S1. Meshed models of honeycomb, schwartz-P, and gyroid structures used for the simulation data.

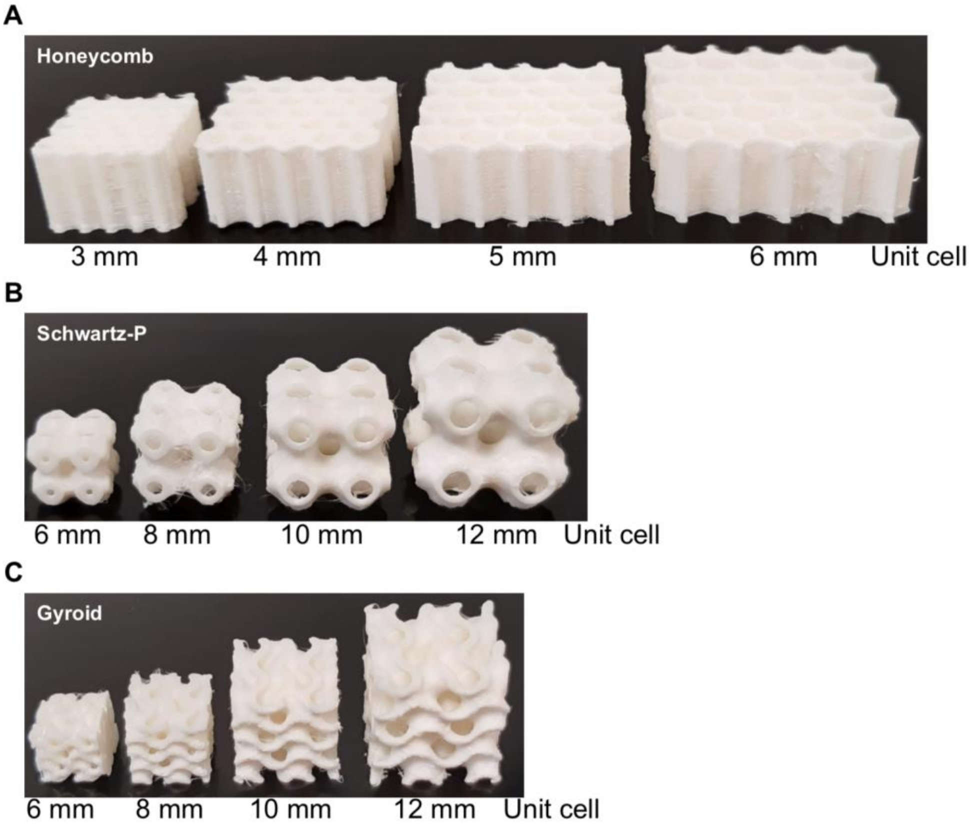

Figure S2. Tunable 3D printed soft lattice scaffolds (A) honeycomb, (B) schwartz-P, and (C) gyroid with optimized printing parameters.

Desposition pathway

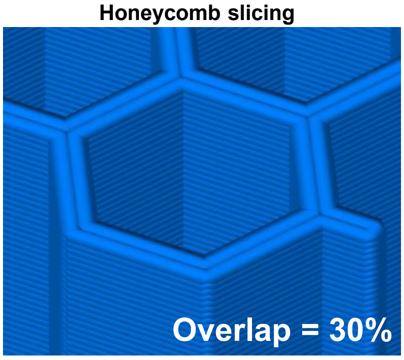

Number of Honeycomb samples	Measurements of 3D printed wall [mm]
1	1,030
2	1,086
3	1,213
4	1,081
5	1,104
6	1,010
7	1,103
8	1,003
9	1,053
10	1,029
Mean [mm]	**1,071**
SD	**0,062**

% Overlap = (2 × Path width [mm]) – Design thickness [mm]) / Design thickness [mm]

Figure S3. Deposition pathway, percentage of overlap and the thickness of the 3D printed walls.

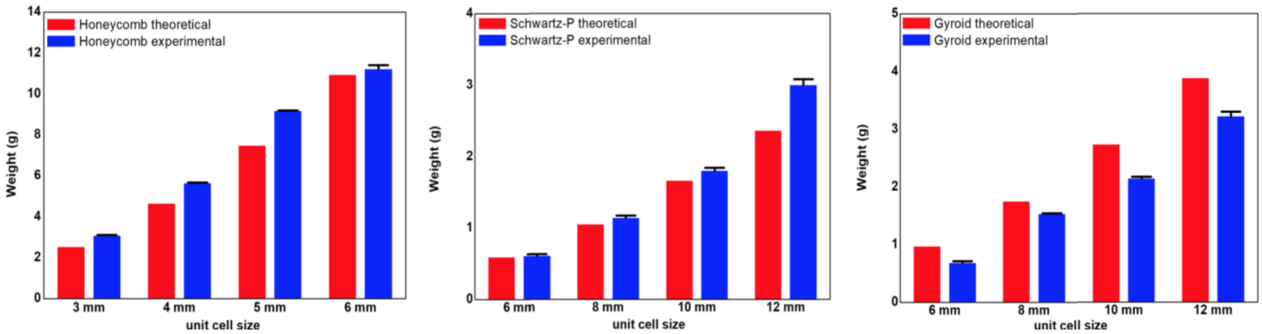

Figure S4. Comparison between the theoretical and experimental weight of 3D printed lattice structures with different geometry and unit cell size.

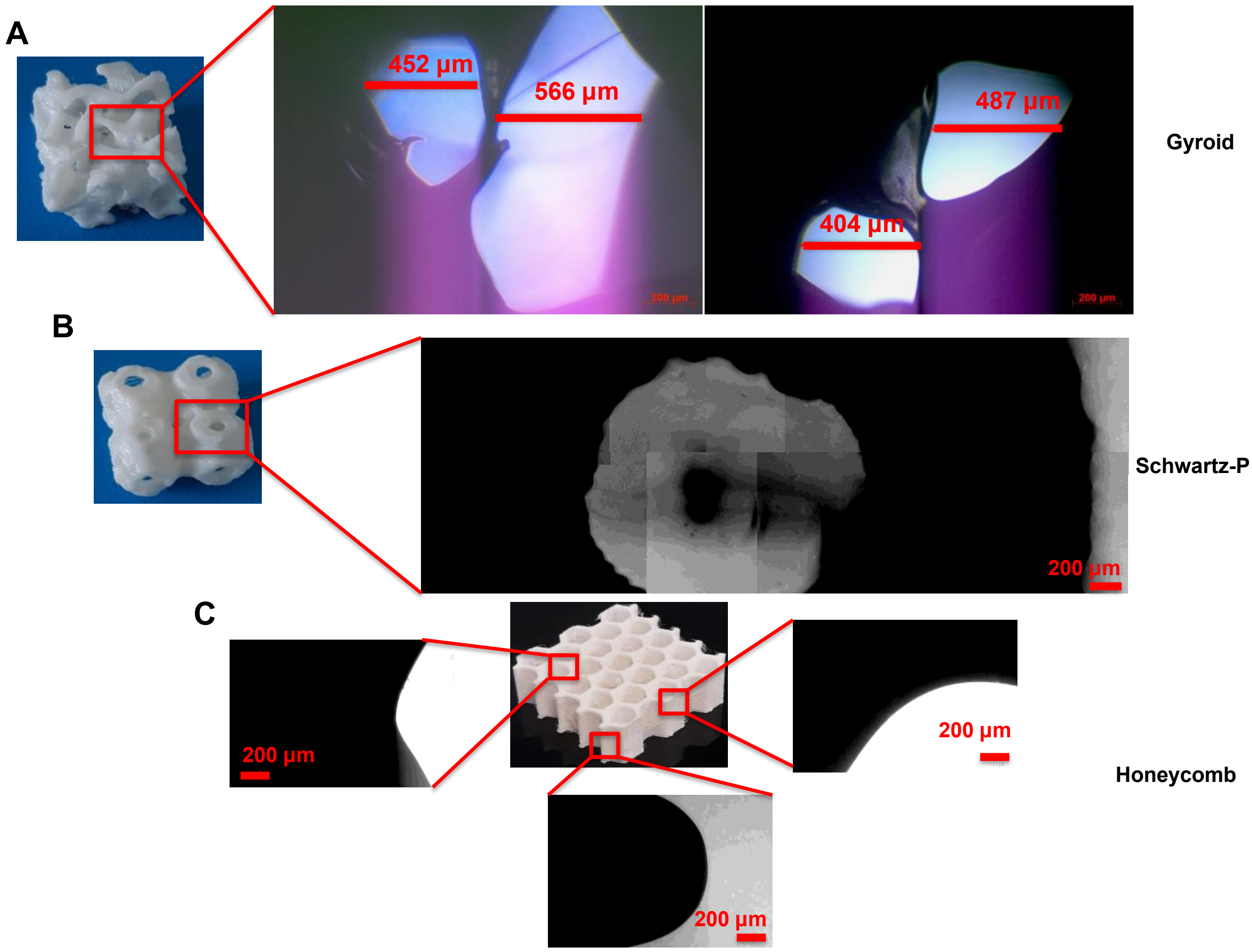

Figure S5. Optical microscopy images of scaffolds cross-section showing (A) micrometric cavitations within the gyroid structures; (B-C) no micrometric cavitations were identified in the schwartz-P and honeycomb structures.

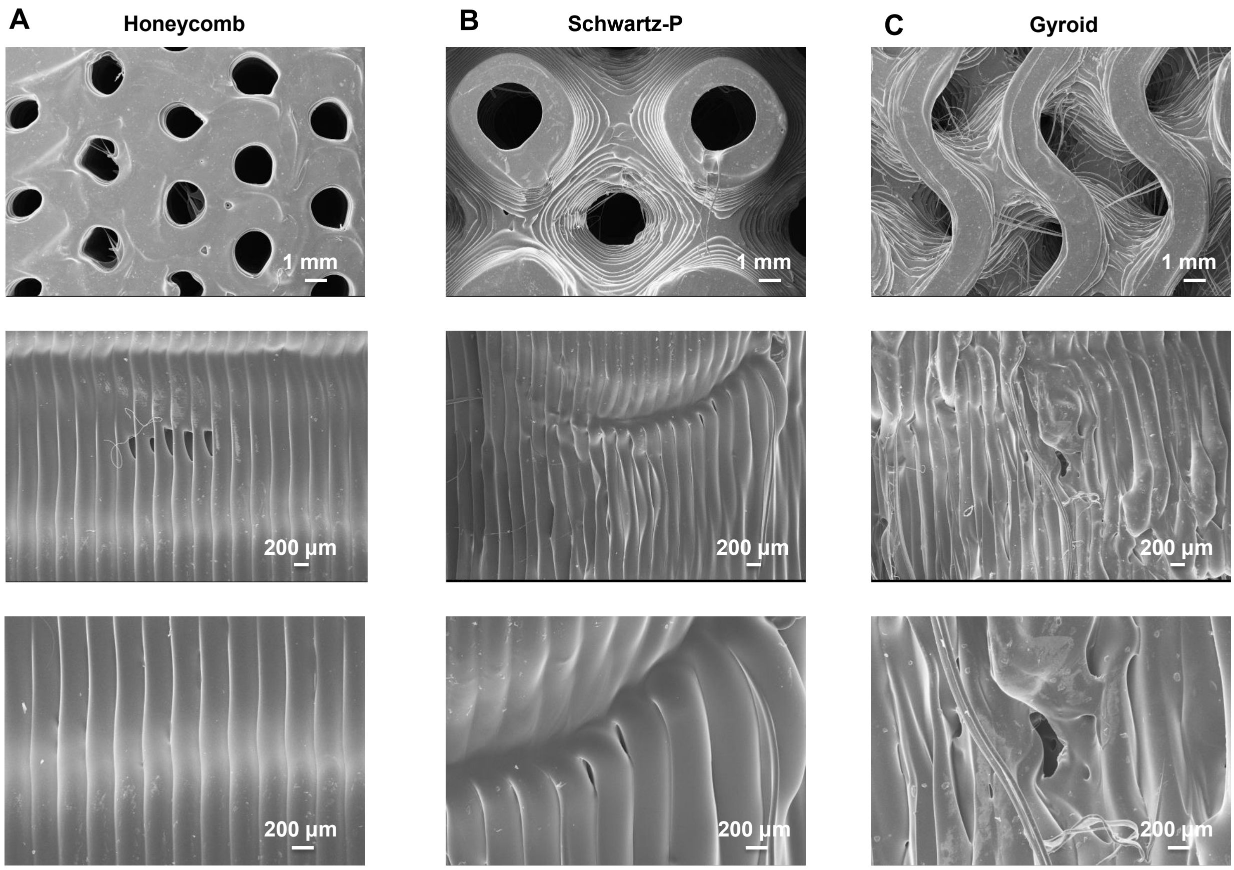

Figure S6. SEM images of (A) honeycomb, (B) schwartz-P, and (C) gyroid structures. No defects such as sagging, improper layer adhesion or porosity are observed in the honeycomb, and schwartz-P structures; whereas microscopic pores are instead present in the gyroid structures.

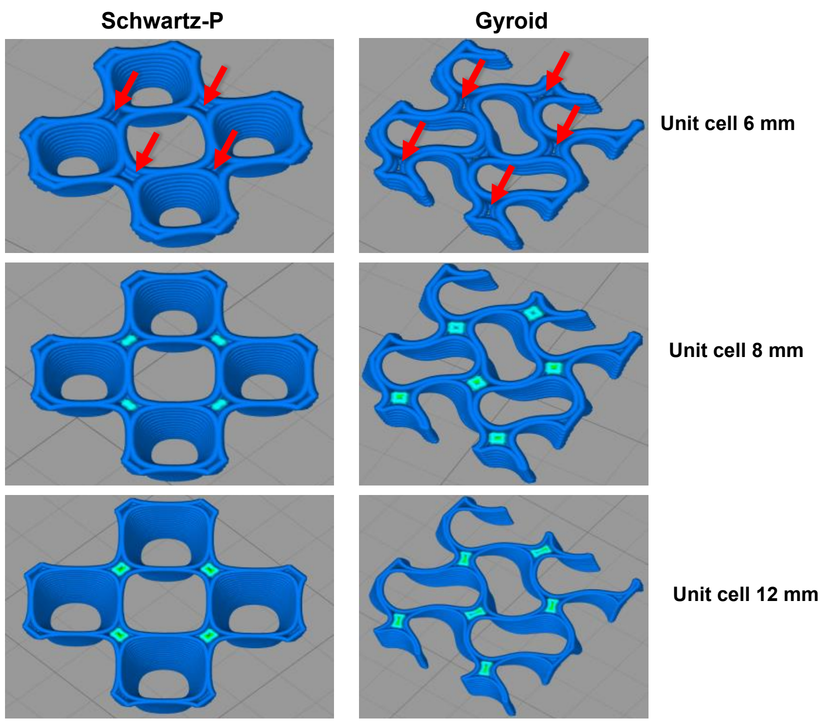

Figure S7. Layers deposition during bridging of TPMS structures with 6, 8, and 12 mm of unit cell size. Red arrows indicate the presence of voids during layer deposition visible only in structures with a unit cell size of 6 mm.

Printing Parameters	H3	H4	H5	H6	SP6	SP8	SP10	SP12	G6	G8	G10	G12
Extruder diameter [mm]	0.4	0.4	0.4	0.4	0.4	0.4	0.4	0.4	0.4	0.4	0.4	0.4
Extruder width [mm]	0.65	0.65	0.65	0.65	0.5	0.5	0.5	0.5	0.5	0.5	0.5	0.5
Extrusion multiplier [-]	1	1	1	1	1	1.1	1.1	1.1	1	1	1	1
Retraction distance [mm]	1	0	0	0	1	1	1	1	1	1	1	1
Retraction speed [mm/min]	2,400	0	0	0	3,000	3,000	3,000	3,000	3,000	3,000	3,000	3,000
Wipe distance [mm]	3	3	3	3	2	2	2	2	0.5	0.5	0.5	0.5
Layer height [mm]	0.15	0.15	0.15	0.15	0.15	0.15	0.15	0.15	0.15	0.15	0.15	0.15
Infill [%]	100	100	100	100	100	100	100	100	100	100	100	100
Support	NO	NO	NO	NO	NO	NO	NO	NO	NO	NO	NO	NO
Nozzle Temperature [°C]	230	230	230	230	230	230	230	230	230	230	230	230
Bed Temperature [°C]	50	50	50	50	50	50	50	50	50	50	50	50
Fan speed [%]	0	0	0	0	20	20	20	20	10	10	10	10
Printing speed [mm/min]	1,100	3,000	3,000	3,000	1,000	2,400	2,400	2,400	1,000	2,400	2,400	2,400
Outline underspeed [%]	70	70	70	70	70	70	70	70	70	70	70	70
Solid underspeed [%]	50	50	50	50	50	50	50	50	50	50	50	50

Table S1. Optimized printing parameters for honeycomb (H), schwartz-P (SP), and gyroid (G) with different unit cell sizes and equal thickness of 1 mm**.**

Honeycomb				Schwartz-P				Gyroid			
Unit cell size (mm)	E_x (MPa)	E_y (MPa)	E_z (MPa)	Unit cell size (mm)	E_x (MPa)	E_y (MPa)	E_z (MPa)	Unit cell size (mm)	E_x (MPa)	E_y (MPa)	E_z (MPa)
3	6.00	5.69	14.79	6	1.57	1.57	1.57	6	4.56	4.51	4.62
4	3.32	3.22	11.42	8	0.79	0.79	0.79	8	2.90	2.86	2.87
5	1.94	1.92	9.05	10	0.61	0.61	0.61	10	2.10	2.05	2.06
6	1.28	1.29	6.28	12	0.44	0.44	0.44	12	1.56	1.52	1.56

Table S2. Comparison of compressive elastic moduli in the *x*, *y*, and *z* directions obtained from the Mooney-Rivlin hyperelastic model of honeycomb, schwartz-P, and gyroid matrix soft lattice scaffolds with different unit cell sizes.